

THE DIVERSE MORPHOLOGIES AND STRUCTURES OF DWARF GALAXIES HOSTING OPTICALLY-SELECTED ACTIVE MASSIVE BLACK HOLES

SETH J. KIMBRELL

eXtreme Gravity Institute, Department of Physics, Montana State University, MT 59715, USA

AMY E. REINES

eXtreme Gravity Institute, Department of Physics, Montana State University, MT 59715, USA

ZACHARY SCHUTTE

eXtreme Gravity Institute, Department of Physics, Montana State University, MT 59715, USA

JENNY E. GREENE

Department of Astrophysical Sciences, Princeton University, Princeton, NJ 08544, USA

AND

MARLA GEHA

Department of Astronomy, Yale University, New Haven, CT 06520, USA

Draft version March 19, 2022

ABSTRACT

We present a study of 41 dwarf galaxies hosting active massive black holes (BHs) using *Hubble Space Telescope* observations. The host galaxies have stellar masses in the range of $M_\star \sim 10^{8.5} - 10^{9.5} M_\odot$ and were selected to host active galactic nuclei (AGNs) based on narrow emission line ratios derived from Sloan Digital Sky Survey spectroscopy. We find a wide range of morphologies in our sample including both regular and irregular dwarf galaxies. We fit the *HST* images of the regular galaxies using GALFIT and find that the majority are disk-dominated with small pseudobulges, although we do find a handful of bulge-like/elliptical dwarf galaxies. We also find an unresolved source of light in all of the regular galaxies, which may indicate the presence of a nuclear star cluster and/or the detection of AGN continuum. Three of the galaxies in our sample appear to be Magellanic-type dwarf irregulars and two galaxies exhibit clear signatures of interactions/mergers. This work demonstrates the diverse nature of dwarf galaxies hosting optically-selected AGNs. It also has implications for constraining the origin of the first BH seeds using the local BH occupation fraction at low masses – we must account for the various types of dwarf galaxies that may host BHs.

1. INTRODUCTION

It is well established that massive galaxies host supermassive black holes (BHs) with masses of $M_{\text{BH}} \sim 10^6 - 10^{10} M_\odot$ at their centers (Kormendy & Ho 2013; Kormendy & Richstone 1995). Our own Milky Way hosts Sagittarius A*, a BH with a mass of $4 \times 10^6 M_\odot$ (Ghez et al. 2008). Much work has gone into studying structural properties, scaling relations, and the possible co-evolution of massive galaxies and the BHs they host (see e.g., the review by Kormendy & Ho 2013). The presence and properties of dwarf galaxies ($M_\star \lesssim 10^{9.5} M_\odot$) hosting massive BHs is not nearly as well studied (see Reines & Comastri 2016; Greene et al. 2019 for reviews), with the first systematic search for these objects performed by Reines et al. (2013).

Lower mass BHs in dwarf galaxies provide a chance to put constraints on BH “seed” masses and probe their possible formation channels (see e.g., Volonteri 2010 and Greene 2012). Mortlock et al. (2011) report observations of a luminous ($6.3 \times 10^{13} L_\odot$) quasar, hosting a $\sim 2 \times 10^9 M_\odot$ BH at a redshift of $z=7.085$ (corresponding

to 0.77 Gyr after the Big Bang). This suggests that the first BH seeds were born in the very early Universe and at least some grew to enormous masses extremely fast. Since we cannot directly observe the small BH seeds at high redshift with current telescopes (Volonteri & Reines 2016; Vito et al. 2017), dwarf galaxies in the low-redshift Universe are our best chance to study BHs that have not grown much compared to the BHs in today’s massive galaxies (Habouzit et al. 2017; Anglés-Alcázar et al. 2017).

In most cases, BHs in dwarf galaxies must be detected as active galactic nuclei (AGN) through radiative signatures, rather than through stellar or gas dynamics (although see Nguyen et al. 2019) since the gravitational sphere of influence of a low-mass BH in a dwarf galaxy is too small to be resolved at distances greater than 4-5 Mpc with current facilities. The first systematic search for AGNs in dwarf galaxies was performed by Reines et al. (2013) using optical spectroscopy from the Sloan Digital Sky Survey (SDSS). They identified 136 dwarf galaxies with narrow emission line ratios indicating the presence of an AGN, some of which also had broad H α emission that was used to estimate BH masses by employing standard viral techniques (e.g., Greene & Ho

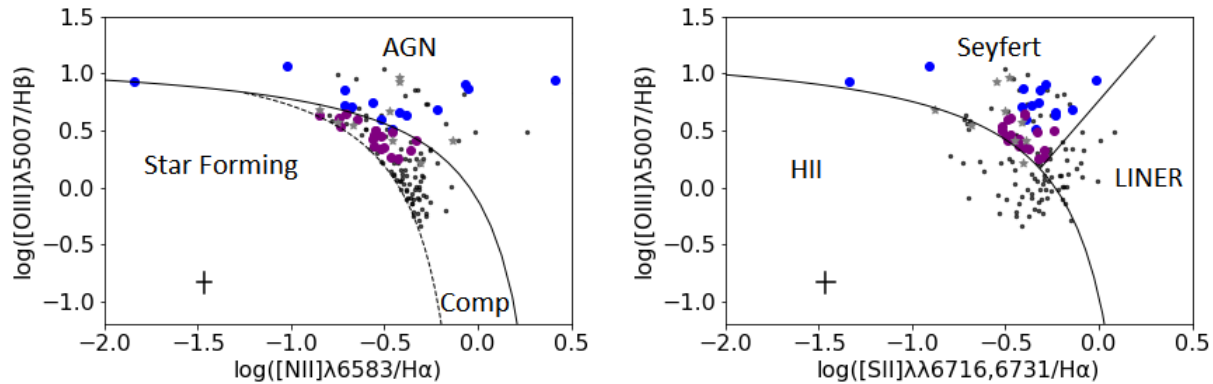


Figure 1. Narrow emission line diagnostic diagrams showing the location of our sample of dwarf galaxies, which exhibit optical signatures of active massive BHs (Reines et al. 2013). Blue and purple points indicate AGNs and Composites, respectively, with new *HST* observations presented here. Grey stars indicate additional galaxies we include in this work from the Reines et al. (2013) sample with *HST* imaging previously presented in Schutte et al. (2019), Baldassare et al. (2017) and Jiang et al. (2011). Black dots indicate the remaining galaxies in the Reines et al. (2013) sample. Left: $[\text{OIII}]/\text{H}\beta$ vs. $[\text{NII}]/\text{H}\alpha$ diagnostic diagram. The solid line shows the “maximum starburst” line from stellar photoionization models (Kewley et al. 2001). The dashed line is an empirical separation between galaxies that show some contribution from AGN and galaxies dominated by star formation (Kauffmann et al. 2003). Composite galaxies fall between the dashed and solid lines, and likely indicate contributions from both an AGN and star formation. Right: $[\text{OIII}]/\text{H}\beta$ vs. $[\text{SII}]/\text{H}\alpha$ diagnostic diagram, using the classifications from Kewley et al. (2006). Typical errors are shown in the lower left corners.

2005). However, as dwarf galaxies have relatively small sizes, very little is known about the detailed morphologies and structures of the host galaxies from ground-based imaging.

In this work, we present *Hubble Space Telescope* (*HST*) imaging of a subset of the Reines et al. (2013) sample. We aim to characterize the structural components of dwarf galaxies hosting active massive BHs and better understand what galactic properties (if any) contribute to or influence the presence of AGNs in dwarf galaxies. We describe our sample of dwarf galaxies and *HST* observations in Sections 2 and 3, respectively. Our structural analysis of the galaxy images is presented in Section 4 and our results are given in Section 5. We present a discussion in Section 6, and end with concluding remarks in Section 7. We adopt a Hubble constant of $H_0 = 73 \text{ km s}^{-1} \text{ Mpc}^{-1}$ throughout this work, and we report magnitudes in the ST system.

2. SAMPLE OF DWARF GALAXIES

The dwarf galaxies with optically-selected AGNs studied here are a subset of objects identified by Reines et al. (2013). Starting with a sample of $\sim 25,000$ emission line galaxies with stellar masses $M_\star \leq 3 \times 10^9 M_\odot$ in the NASA-Sloan Atlas (NSA), Reines et al. (2013) analyzed Sloan Digital Sky Survey (SDSS) spectra of these objects and found 136 dwarf galaxies exhibiting optical signatures of accreting massive BHs. These galaxies fall in either the AGN or Composite region of the $[\text{OIII}]/\text{H}\beta$ vs. $[\text{NII}]/\text{H}\alpha$ narrow emission line diagnostic diagram (i.e., the BPT diagram; Baldwin et al. (1981); Kewley et al. (2001)). Our target galaxies were also selected to be in the Seyfert region of the $[\text{OIII}]/\text{H}\beta$ vs. $[\text{SII}]/\text{H}\alpha$ narrow emission line diagnostic diagram, making them among the strongest cases of dwarf galaxies hosting massive BHs. However, it is worth noting that low-metallicity AGNs and low-metallicity starbursts both fall in the upper left region of the BPT diagram and are therefore difficult to distinguish (i.e., RGG 5, the leftmost point in Figure 1; also see the discussion in Section 6.3).

We proposed for *HST* SNAP observations of 61 dwarf galaxies meeting the criteria above and 33 were ultimately observed for this program. Of these, 13 galaxies were classified as AGNs by Reines et al. (2013) and 20 were classified as Composites. Two of these galaxies, RGG 20 and RGG 118, are broad-line AGNs with virial BH masses of $M_{\text{BH}} \sim 10^{6.1} M_\odot$ (Reines et al. 2013) and $M_{\text{BH}} \sim 10^{4.7} M_\odot$ (Baldassare et al. 2015), respectively.

BH mass estimates for the narrow-line objects are in the range of $M_{\text{BH}} \sim 10^{4.9} - 10^{5.8} M_\odot$ based on the AGN scaling relation between BH mass and total galaxy stellar mass from Reines & Volonteri (2015). Total stellar masses from the NSA are in the range $M_\star \sim 10^{8.5} - 10^{9.5} M_\odot$, and come from the *kcorrect* code of Blanton & Roweis (2007).

We also include 7 additional dwarf galaxies with broad-line AGNs and Composites from Reines et al. (2013) that have *HST* observations from another program (PI: Reines, Proposal ID 13943). Virial BH masses for these objects are in the range $M_{\text{BH}} \sim 10^{4.9} - 10^{6.1} M_\odot$ (Reines et al. 2013) and these AGNs have been confirmed with *Chandra* X-ray observations (Baldassare et al. 2017). The *HST* near-IR data are analyzed by Schutte et al. (2019), who also give an updated BH-bulge mass relation including dwarf galaxies. Here we include the galaxy structural information presented in Schutte et al. (2019). We also include 1 additional broad-line object (RGG 123) from Reines et al. (2013) that has *HST* observations and structural analysis presented in Jiang et al. (2011), bringing our total sample to 41 BH-hosting dwarf galaxies with high quality *HST* images.

Figure 1 shows narrow-line diagnostic diagrams with locations of our sample galaxies using the line measurements in Reines et al. (2013). Figure 2 shows the stellar masses, absolute magnitudes, colors, redshifts, half-light radii and g-band surface brightnesses of our galaxies compared to the entire Reines et al. (2013) sample, which illustrates that we have a representative sample of the RGG galaxies in this work. In order to have uniform surface brightness measurements, we use data from the

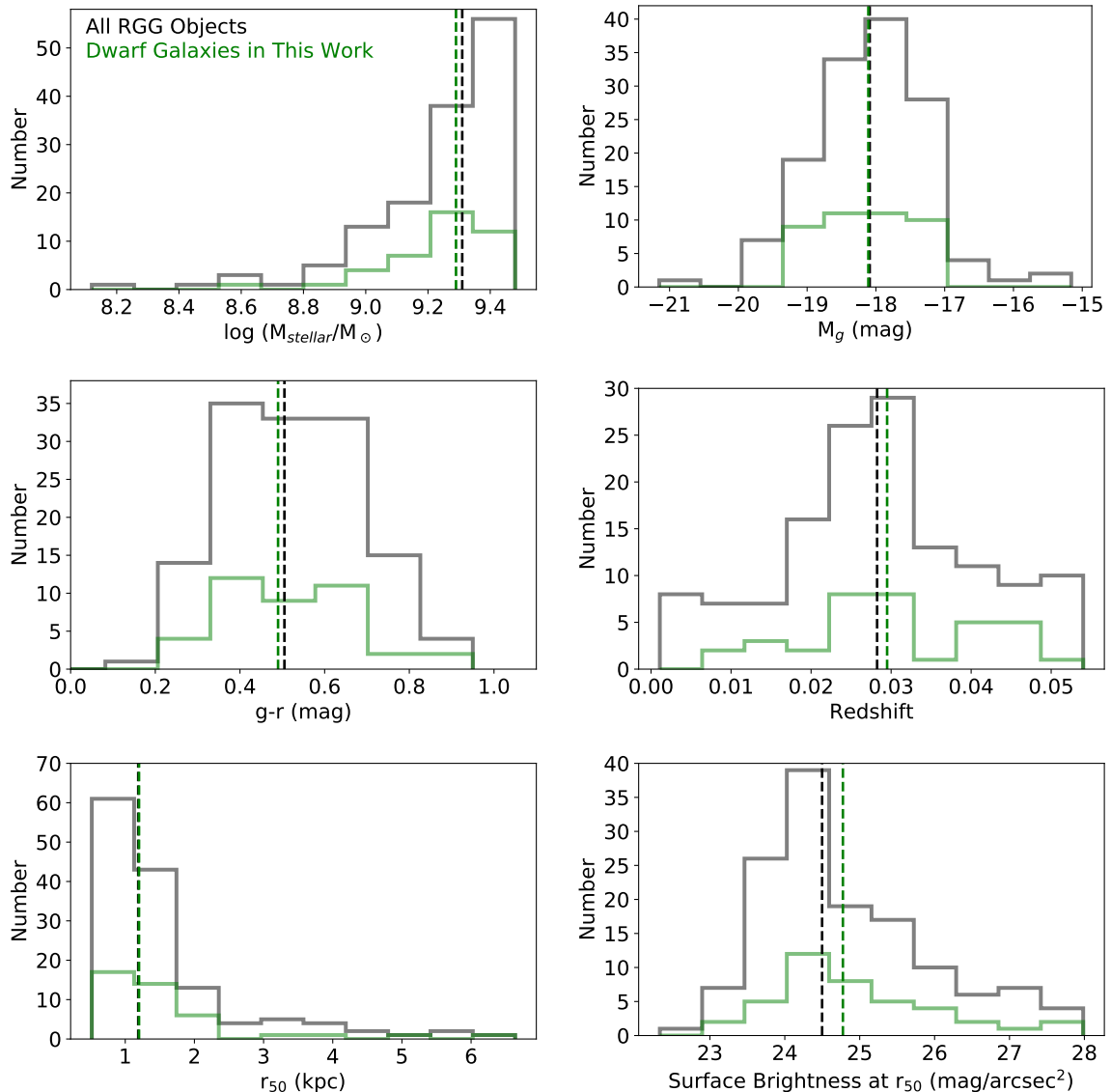


Figure 2. Distribution of stellar mass, absolute g -band magnitude, $g - r$ color, redshift, Petrosian half-light radius and interpolated g -band surface brightness at the Petrosian half-light radius for the galaxies in this work (green histograms). Properties of the entire Reines et al. (2013) (RGG) sample are shown as gray histograms. Dashed lines indicate median values.

NSA giving surface brightnesses at discrete radii and use a spline interpolation to estimate the surface brightness at the Petrosian half-light radius for all the galaxies in the RGG sample, including the ones analyzed in this work. Table 1 lists our sample of dwarf galaxies and their properties.

3. HUBBLE SPACE TELESCOPE OBSERVATIONS

HST near-infrared images of the 33 dwarf galaxies observed for our SNAP program were obtained with the Wide Field Camera 3 (WFC3) between 2015 October 11 and 2017 June 18 (PI Reines; Proposal ID 14251). The observations were taken in the IR/F110W filter (wide YJ -band) with a central wavelength of $1.15 \mu\text{m}$.

Snapshot observations of each galaxy were taken with a total on-source exposure time of ~ 16 minutes. We utilized a four-point sub-pixel dither pattern and used

a 512×512 pixel subarray to avoid buffer dumps. The subarray has a field of view of $65.5'' \times 65.5''$ and all of our galaxies fall well within the array.

The images were processed by the STScI data reduction pipeline using the AstroDrizzle routine. The final cleaned, combined and calibrated images have an angular resolution of $\sim 0''.13$ (FWHM), corresponding to a range in physical scales of $\sim 17 - 131$ pc, and a scale of ~ 70 pc at the median distance of our sample (111 Mpc).

4. ANALYSIS

The primary goal of this work is to characterize the structures of dwarf galaxies hosting optically-selected AGNs. For galaxies with regular morphologies, our general approach is to model each galaxy with a PSF plus either one or two Sérsic components for the galaxy light. For the galaxies requiring two Sérsic components, these

Table 1
Sample of 41 Dwarf Galaxies Hosting Optically-Selected AGNs with *HST* Observations

| RGG ID (1) | NSAID (2) | SDSS Name (3) | z (4) | $g - r$ color (5) | M_g (6) | $\log M_*$ (7) |
|----------------------------|--------------|---------------------|------------|----------------------|--------------|-------------------|
| AGNs | | | | | | |
| <i>RGG 1^a</i> | 62996 | J024656.39−003304.8 | 0.0462 | 0.81 | −17.99 | 9.5 |
| RGG 2 | 7480 | J024825.26−002541.4 | 0.0247 | 0.58 | −17.32 | 9.1 |
| RGG 4 | 64339 | J081145.29+232825.7 | 0.0157 | 0.36 | −17.98 | 9.0 |
| RGG 5 | 46677 | J082334.84+031315.6 | 0.0098 | −0.29 | −18.85 | 8.5 |
| RGG 6 | 105376 | J084025.54+181858.9 | 0.0150 | 0.59 | −17.61 | 9.3 |
| RGG 7 | 30020 | J084204.92+403934.5 | 0.0293 | 0.62 | −17.45 | 9.3 |
| <i>RGG 9^a</i> | 10779 | J090613.75+561015.5 | 0.0469 | 0.40 | −18.98 | 9.3 |
| RGG 10 | 106134 | J092129.98+213139.3 | 0.0313 | 0.58 | −18.20 | 9.3 |
| <i>RGG 11^a</i> | 125318 | J095418.15+471725.1 | 0.0328 | 0.44 | −18.73 | 9.2 |
| RGG 15 | 27397 | J110912.37+612347.0 | 0.0068 | 0.36 | −17.33 | 8.9 |
| RGG 16 | 30370 | J111319.23+044425.1 | 0.0265 | 0.49 | −17.98 | 9.3 |
| <i>RGG 20</i> | 52675 | J122342.82+581446.4 | 0.0144 | 0.66 | −18.11 | 9.5 |
| RGG 22 | 77431 | J130434.92+075505.0 | 0.0480 | 0.45 | −18.77 | 9.0 |
| RGG 26 | 54572 | J134939.36+420241.4 | 0.0411 | 0.47 | −18.55 | 9.3 |
| RGG 28 | 70907 | J140510.39+114616.9 | 0.0174 | 0.42 | −18.13 | 9.4 |
| RGG 29 | 71023 | J141208.47+102953.8 | 0.0326 | 0.42 | −17.74 | 9.1 |
| <i>RGG 32^a</i> | 15235 | J144012.70+024743.5 | 0.0295 | 0.31 | −19.18 | 9.3 |
| Composites | | | | | | |
| RGG 37 | 6059 | J010005.93−011058.8 | 0.0514 | 0.59 | −18.76 | 9.3 |
| RGG 40 | 82616 | J074829.21+510052.4 | 0.0190 | 0.38 | −17.89 | 9.1 |
| <i>RGG 48^a</i> | 47066 | J085125.81+393541.7 | 0.0411 | 0.28 | −19.19 | 9.1 |
| RGG 50 | 47918 | J090737.05+352828.4 | 0.0276 | 0.53 | −18.53 | 9.4 |
| RGG 53 | 105953 | J091720.88+191018.9 | 0.0285 | 0.87 | −17.17 | 9.3 |
| RGG 56 | 26850 | J093239.45+511542.9 | 0.0473 | 0.38 | −18.99 | 9.2 |
| RGG 58 | 39968 | J093821.54+063130.8 | 0.0224 | 0.48 | −18.05 | 9.4 |
| RGG 59 | 39954 | J094705.72+050159.8 | 0.0242 | 0.47 | −17.73 | 9.2 |
| RGG 64 | 106991 | J100423.33+231323.4 | 0.0266 | 0.49 | −17.53 | 9.1 |
| RGG 66 | 55081 | J101747.09+393207.7 | 0.0540 | 0.51 | −18.92 | 9.0 |
| RGG 67 | 12623 | J102149.12+635206.8 | 0.0211 | 0.62 | −16.99 | 9.0 |
| RGG 69 | 117416 | J102833.33+184513.9 | 0.0274 | 0.58 | −17.98 | 9.5 |
| RGG 79 | 19138 | J112957.62+653804.8 | 0.0439 | 0.56 | −18.21 | 9.5 |
| RGG 81 | 93958 | J113129.20+350958.9 | 0.0337 | 0.95 | −17.24 | 9.3 |
| RGG 86 | 66343 | J115359.06+130853.6 | 0.0226 | 0.67 | −17.59 | 9.3 |
| RGG 88 | 52494 | J115812.53+575322.1 | 0.0415 | 0.50 | −18.18 | 9.3 |
| RGG 89 | 32762 | J115922.33+511809.2 | 0.0297 | 0.78 | −17.32 | 9.3 |
| RGG 94 | 161692 | J122505.40+051945.9 | 0.0066 | 0.67 | −17.27 | 9.3 |
| <i>RGG 118^b</i> | 166155 | J152303.80+114546.0 | 0.0243 | 0.37 | −18.38 | 9.4 |
| <i>RGG 119^a</i> | 79874 | J152637.36+065941.6 | 0.0382 | 0.25 | −18.65 | 9.4 |
| <i>RGG 123^c</i> | 18913 | J153425.58+040806.6 | 0.0395 | 0.35 | −18.16 | 9.1 |
| <i>RGG 127^a</i> | 99052 | J160531.84+174826.1 | 0.0317 | 0.61 | −17.46 | 9.4 |
| RGG 135 | 4308 | J173202.96+595855.0 | 0.0291 | 0.39 | −18.91 | 9.4 |
| RGG 136 | 5563 | J235609.14−002428.6 | 0.0256 | 0.31 | −18.68 | 9.2 |

Note. — Column 1: identification number given in Reines et al. (2013). Column 2: NSA identification number. Column 3: SDSS name. Column 4: redshift. Column 5: $g - r$ color from the NSA. Column 6: Absolute g -band magnitude from the NSA. Column 7: Log total stellar mass from the NSA in units of M_\odot . Italicized RGG IDs indicate broad-line AGNs, for which the virial mass has been determined using broad H α emission (Reines et al. 2013; Baldassare et al. 2015 for RGG 118).

^a Structural analysis adopted from Schutte et al. (2019).

^b Structural analysis adopted from Baldassare et al. (2017).

^c Structural analysis adopted from Jiang et al. (2011).

structures can be ascribed to an inner bulge/pseudobulge component plus an outer disk component. In general, we do not attempt to model more complex structures, such as spiral arms or tidal features, although we include bars in a few cases. In dwarf galaxies, these features tend to be very faint and difficult to model, despite being fairly obvious to the eye. In the subsections below, we describe the details of our modeling and analysis.

Six of our galaxies are irregular in shape and fitting these galaxy images with axisymmetric models proved impractical. We present the dwarf irregular galaxies in Section 5.2.

4.1. PSF Construction

It is important to use an accurate PSF to model the detector response to a point source, given that these galaxies are selected as AGN hosts. A PSF which does not properly capture that response can lead to inaccurate modeling of the galaxy as a whole.

We used stars in our images to create PSFs. Since the response of a detector to a point source is dependent on location on the detector, we selected images with a bright star within 100 pixels of the center of the galaxy. Three stars met this criterion (one each in the images of RGG 2, RGG 22 and RGG 64).

We took a cutout of these stars and performed a flux-

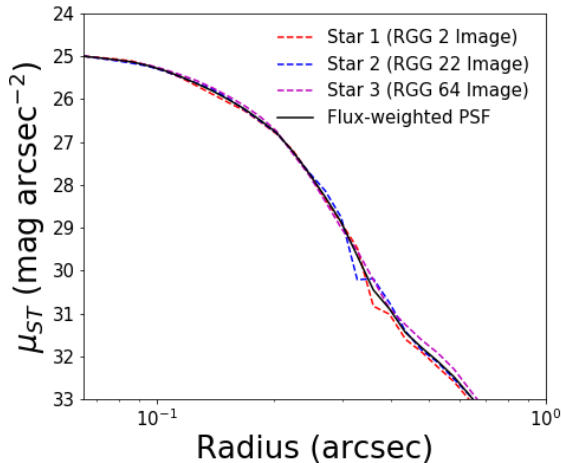


Figure 3. Radial intensity profiles for the bright central stars in RGG 2, RGG 22 and RGG 64, as well as the flux weighted average PSF.

weighted average to create one image. We then made a model of the resulting image, giving us a PSF that is the result of averaging individual stars, while having the high signal-to-noise ratio required of PSFs. The PSF we created, as well as the profiles of each of the three stars, can be seen in Figure 3. We used this PSF for all of our modeling.

4.2. Galaxy Modeling

We fit two-dimensional surface brightness models to our images using the galaxy fitting software GALFIT (Peng et al. 2010). GALFIT has many analytical models which can be used to fit galaxies. For this work, we used the very general Sérsic profile, which takes the form (Sérsic 1963):

$$\Sigma(r) = \Sigma_e \times \exp \left[-\kappa \left(\left(\frac{r}{r_e} \right)^{\frac{1}{n}} - 1 \right) \right] \quad (1)$$

where r_e is the effective radius defined such that half of the flux lies within r_e , and Σ_e is the surface brightness at r_e . The parameter n , which is coupled to κ , is the Sérsic index; a higher Sérsic index indicates a steep inner brightness profile and more extended wings, while a lower index indicates a shallower profile at small radius and less extended wings. κ is a free parameter defined as $\kappa = \Gamma(2n)/2$, where Γ is the complete gamma function. The case of $n = 4$ is the de Vaucouleurs profile, often used to model classical bulges (de Vaucouleurs 1948). Values of $n = 1$ and $n = 0.5$ describe exponential disks and Gaussian profiles, respectively.

Our galaxy fitting process followed that recommended by Peng et al. (2010). Before running GALFIT, we first created mask files containing the pixel coordinates of prominent foreground and background objects we wished to ignore during the modeling process. We then began by using a single Sérsic component only.

We found that, in every case, a single Sérsic component was a poor fit and left very bright residuals. However, this gave us a rough estimate for some basic properties such as size and axis ratio of a given galaxy. We then

added a central PSF to the single Sérsic model, using the results of the previous fit as our starting parameters. This PSF could represent the AGN and/or an unresolved nuclear star cluster (see §6.2).

We then attempted to model each galaxy with two Sérsic components without a central point source. We let the Sérsic component of the inner component vary, while holding the Sérsic index of the outer component fixed at the canonical value for an exponential disk of $n = 1$. This again gave us some basic information about the bulge/disk model (e.g., relative sizes) but it rarely resulted in a good fit. We then added a point source to the two-Sérsic model.

For three of the galaxies in our SNAP program, RGG 7, RGG 29 and RGG 37, a bar was necessary. This was determined through visual inspection of the data, in which the residuals showed a bright bar through the center of the galaxy that was missed by our basic model. RGG 127 also required a bar (Schutte et al. 2019).

In general, when GALFIT found a best-fit model, we re-fit the galaxy several times while varying the starting parameters to ensure that the software was not just falling into a local minimum of goodness of fit.

4.3. Model Selection

Next we determined whether each galaxy was best fit by one Sérsic component or two Sérsic components (with one being an exponential disk), plus a PSF. To decide this, we followed the example of Oh et al. (2017) and used a three-step model selection process. First, we eliminated the two Sérsic model if the effective radius of the exponential disk was smaller than the effective radius of the inner component. Next, we eliminated the two Sérsic model if the disk was subdominant everywhere in the radial profile. Finally, we used the Akaike Information Criterion (AIC) (Akaike 1974). Assuming normally distributed noise, the AIC is calculated from χ^2 as:

$$\text{AIC} = \chi^2 + 2k \quad (2)$$

where k is the number of free parameters in a model. Following Oh et al. (2017), we eliminated the two Sérsic model if adding more parameters did not reduce the AIC by ≥ 10 . We report the results in §5.

We note that the faintest features we modeled reach a surface brightness of ~ 25 mag/arcsec². It is possible that, for some of the least luminous galaxies in our sample, *HST* could fail to detect features fainter than this in the diffuse outer regions of the galaxy. This could have an impact on the modeling procedure and model selection described above.

4.4. Testing PSF Necessity

We also tested whether the point sources are necessary components in our models, given that some are subdominant to the galactic components (e.g. RGG 69). We used the AIC as our first criterion; as in §4.3, we rejected the model including a PSF if it does not reduce the AIC by ≥ 10 . Using this criterion, all of the galaxies we modeled preferred the inclusion of a PSF.

As additional checks on the necessity of the PSFs, we also examined the Sérsic indices of the inner components and the residuals. Kormendy & Ho (2013) set an upper bound for the Sérsic index of dwarf ellipticals at $n \lesssim 4$,

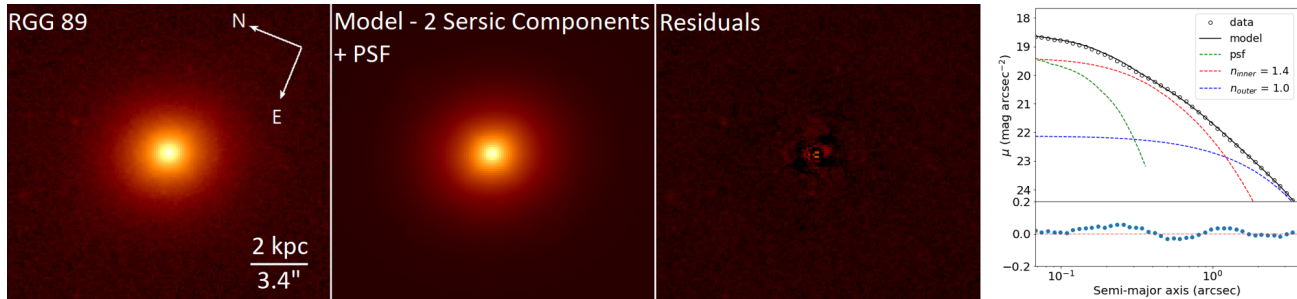


Figure 4. Left three panels: *HST*/WFC3 F110W image of RGG 89, GALFIT model, and the residuals after subtracting the model from the image. Images are shown on a stretched log scale to show faint details in the residuals. The data are shown as black circles and the model is shown as a black line. The individual model components are shown as colored dashed lines. The residuals are shown in the bottom panel.

and bounds for pseudobulges and classical bulges at $n \lesssim 2$ and $n \gtrsim 2$, respectively. Other studies performing *HST* photometry of dwarf galaxies and low-mass AGN hosts (e.g. Jiang et al. 2011; Schutte et al. 2019; Graham & Guzmán 2003) find (pseudo)bulges and dwarf ellipticals with $n \leq 4$. Therefore, we were skeptical of models without a PSF if they led to an inner Sérsic index much larger than this (i.e., $n \geq 5$).

Finally, we visually examined the residuals after subtracting the GALFIT model from the data. A Sérsic component attempting to account for a missing PSF leads to telltale rings in the residuals, alternating bright and dark, in the center of the galaxy. Therefore, we also rejected models without PSFs if they led to these rings.

To summarize, of the 26 regular galaxies modeled in our SNAP sample, all 26 preferred the model which includes a PSF based on the AIC. In addition, 9 have Sérsic indices $n \geq 5$ when a PSF is not included, and 21 have rings in the residuals when a PSF is not included (some have both a high Sérsic index and rings in the residuals). Only 3 out of the 26 galaxies (RGG 2, RGG 59 and RGG 88) preferred the PSF model solely based on the AIC. While the presence of a point source is less certain in these three galaxies, we nevertheless adopted the PSF model for consistency with the rest of the sample.

4.5. Uncertainty Calculation

Uncertainties in the GALFIT parameters were found following the example of Baldassare et al. (2017). Magnitudes are most sensitive to changes in the sky background, while effective radii and Sérsic indices are most sensitive to the point spread function. Using sigma clipping, we iteratively subtracted points that were 3σ above the median of each full image to estimate a sky background and, once GALFIT converged on fit parameters for a model, we replaced the fit sky background with the estimated one. We used the change in magnitudes as our error. To determine the uncertainty in effective radii and Sérsic index, we replaced the PSF constructed from averaging three central stars with one constructed from a single bright central star. The changes in effective radius and Sérsic index were used as our error.

4.6. Surface Brightness Profiles

Using the *isophote* Python package, we fit elliptical isophotes to the data and our GALFIT models. With these isophotes, we constructed 1-D surface brightness

profiles. We used these 1-D profiles as additional checks on our models. Figure 4 shows an example of a GALFIT model and surface brightness profile for the dwarf galaxy RGG 89. Similar plots for the other galaxies in our sample are shown in the Appendix. The images are stretched on a log scale to show very faint details. While there are features in the residuals for some of the galaxies, they are quite dim and will not significantly affect our results. Typically, the residuals are $\lesssim 0.1$ mag arcsec⁻².

5. RESULTS

Of the 41 AGN-hosting dwarf galaxies in our sample, the vast majority ($35/41 = 85\%$) have fairly regular morphologies and can be adequately modeled in GALFIT using one or two Sérsic components plus a PSF, and sometimes a bar (§5.1). A smaller, but non-negligible, fraction of the dwarf galaxies in our sample ($6/41 = 15\%$) have irregular/disturbed morphologies and were not successfully modeled in GALFIT. These galaxies are presented in §5.2.

5.1. Dwarf Galaxies With Regular Morphologies

We have determined whether a single Sérsic or two Sérsic model is a better fit for the regular galaxies in our sample (including the galaxies taken from the literature as described in §2 and noted in Table 1). A PSF component is required in all cases to account for the central AGN light and possibly an unresolved nuclear star cluster. The GALFIT results are summarized in the Appendix in Table 2. An example *HST* image, model fit and surface brightness profile is shown in Figure 4. Corresponding figures for the other galaxies with regular morphologies can be found in the Appendix here (or see Schutte et al. 2019, Baldassare et al. 2017, Jiang et al. 2011.)

We find that 74% (26/35) of the regular galaxies in our sample are best fit by a two-component Sérsic model where we ascribe the outer component to a disk with fixed $n = 1$. The other 26% (9/35) of the regular galaxies in our sample are best fit with a single Sérsic model.

For these single Sérsic galaxies, we distinguish between (pseudo)bulge/elliptical galaxies and disk-like galaxies using the Sérsic index; galaxies with $n \geq 1.5$ are designated (pseudo)bulges/ellipticals, while galaxies with $n < 1.5$ are disk-like (see Figure 5).

5.1.1. Disk Properties

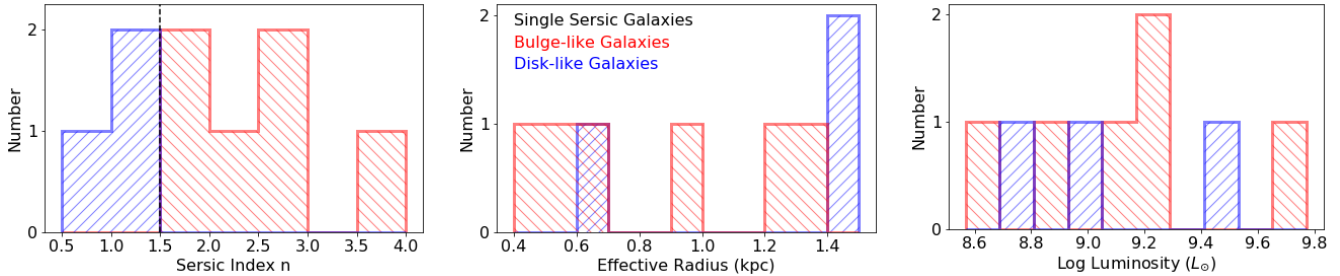


Figure 5. Left: Distribution of the Sérsic indices for the one-Sérsic galaxies in our sample. A vertical dashed line shows the cutoff between disk-like galaxies and (pseudo)bulge-like galaxies. Disk-like galaxies are shown in blue histograms, while (pseudo)bulge-like galaxies are shown in red histograms. Middle: Distribution of the effective radii (in kpc), with the same color scheme as the left. Right: Distribution of the luminosities (in WFC3/IR F110W; $1.15\mu\text{m}$), with the same color scheme as the left.

The galaxies in our sample tend to be disk-dominated. For the galaxies best fit with two Sérsic components, the median bulge-to-total (B/T) ratio (with PSF subtracted) is $\langle B/T \rangle = 0.21$ with a range of $B/T \sim 0.04 - 0.88$. Figure 6 shows the distribution of B/T ratios. Galaxies modeled with a single Sérsic component consistent with a (pseudo)bulge are shown in Figure 6 as having a B/T ratio of 1, and single Sérsic galaxies consistent with a disk have $B/T = 0$. Luminosities of individual components were calculated from the apparent magnitudes reported by GALFIT and the distance to each galaxy. The half-light radii of the disks in our sample span a range of $r_{e,\text{disk}} \sim 0.7 - 6.5$ kpc, with a median of $r_{e,\text{disk}} \sim 2.2$ kpc. The left column of Figure 7 shows the distributions of $r_{e,\text{disk}}$ and L_{disk} .

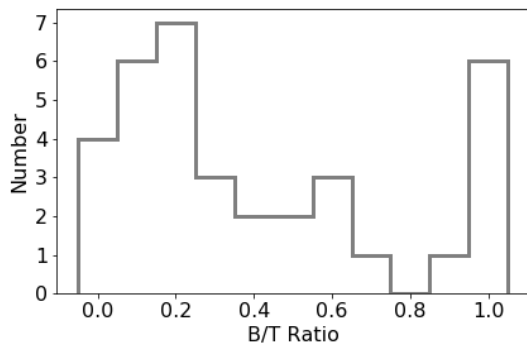


Figure 6. Distribution of bulge-to-total light ratios for all the galaxies in our sample (one-Sérsic and two-Sérsic galaxies). A B/T of 0 indicates a disk-like single-Sérsic galaxy, while a B/T ratio of 1.0 indicates a (pseudo)bulge single-Sérsic galaxy.

In addition to the 26 galaxies which have a disk and a (pseudo)bulge, 3 additional galaxies (RGG 7, 29 and 123) are best modeled with a single Sérsic component and appear to be disks without detectable (pseudo)bulges. However, it should be noted that RGG 7 and RGG 29 each have a bar in addition to the disk component, and RGG 7 also has spiral structure in the disk, which we do not model. There is also a bright point source at the center of these galaxies and it is possible we could have missed a very small bulge component (or nuclear star cluster), even with *HST* resolution.

Additionally, RGG 15 is notable for being completely dominated by the disk at all radii except for the central

PSF (see Figure 14 in Appendix), although we do detect a small and faint inner Sérsic component with $n = 0.5$. The half-light radius of the inner component is only ~ 0.3 kpc, compared to ~ 2 kpc for the disk. The inner component is also 3.5 magnitudes fainter than the disk of this galaxy.

5.1.2. (Pseudo)bulge Properties

Given the importance of BH-to-bulge scaling relations (see, e.g., Kormendy & Ho 2013), it is vital to determine if our galaxies possess some kind of (pseudo)bulge component. In our sample of dwarf galaxies, we aim to distinguish between pseudobulges and classical bulges. Structurally, pseudobulges have more of an exponential profile than classical bulges, somewhat resembling an inner disk. The Sérsic index acts as an effective selector of pseudobulges versus classical bulges - pseudobulges have Sérsic indices $n \lesssim 2$ (see e.g., Fisher & Drory 2008; Kormendy & Kennicutt 2004 for more on the differences between pseudobulges and classical bulges).

Based on above criterion, 21 of the 26 regular galaxies best fit with two Sérsic components have an inner component consistent with a (pseudo)bulge, while 5 host a more classical bulge.

When including the 6 single Sérsic galaxies that are consistent with being bulge-like, the total number of galaxies hosting a (pseudo)bulge comes to 32/41 (78%). Despite most of our galaxies hosting some kind of (pseudo)bulge component, Figure 6 shows that they tend to be disk-dominated (§5.1.1).

The Sérsic indices of the inner/(pseudo)bulge components for the two-Sérsic galaxies are in the range of $n_{\text{bulge}} \sim 0.3 - 4.0$, with a median of $\langle n_{\text{bulge}} \rangle = 1.3$ (see Figure 8). The single Sérsic galaxies that are bulge-like have relatively large Sérsic indices compared to the inner components of galaxies best fit by a (pseudo)bulge-disk decomposition.

The inner/(pseudo)bulge components in our dwarf galaxy sample tend to be quite compact. The half-light radii are in the range $r_{e,\text{bulge}} \sim 0.1 - 1.6$ kpc, with a median of $\langle r_{e,\text{bulge}} \rangle \sim 0.3$ kpc. The most compact galaxy overall in our sample is RGG 29, a galaxy best fit with a single Sérsic component with $n = 1.4$ and $r_e \sim 0.5$ kpc.

The middle column of Figure 7 shows the distributions of $r_{e,\text{bulge}}$ and L_{bulge} .

The angular diameters ($2r_{e,\text{bulge}}$) of the (pseudo)bulges in our sample are shown in Figure 8. The median value is $1''.2$ and the range in angular diameter is $0''.1 - 6''.5$. This

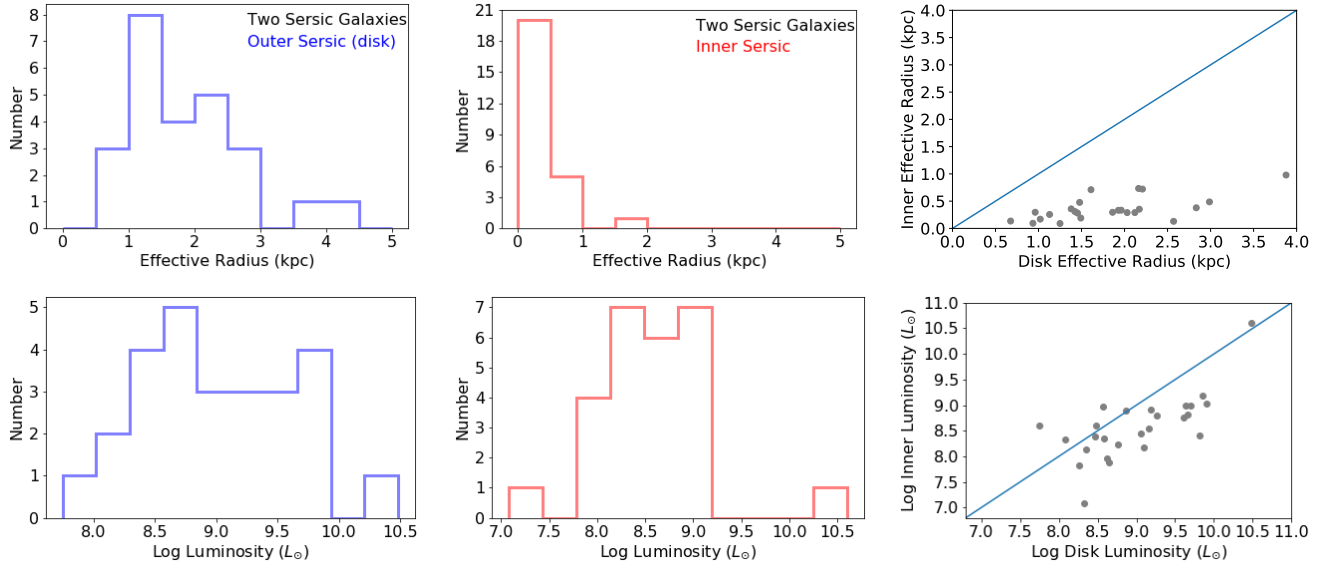


Figure 7. Disk and (pseudo)bule properties determined from GALFIT, for galaxies best fit with two Sérsic components. Left column from top to bottom: Disk effective radii (in kpc) and luminosities (in WFC3/IR F110W; $1.15\mu\text{m}$). RGG 118, which has a disk effective radius of 6.5 kpc, is not shown in the left top panel. RGG 118 and RGG 123 are not included in the luminosity distribution in the lower left panel as the *HST* observations were taken in the WFC3/IR F160W and WFPC2 F814W filters, respectively. Middle column: Same as left column but for the inner Sérsic. Right column: (Pseudo)bule versus disk properties for individual galaxies, along with the one-to-one line for comparison. Typical errors in the radii and luminosities are smaller than the points (see §4.5 for discussion of error calculation and Table 2 for reported errors).

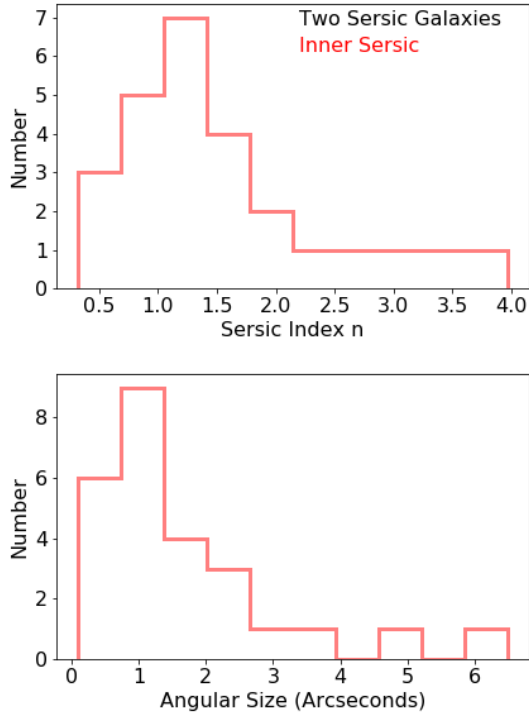


Figure 8. Top: distribution of the Sérsic indices for the (pseudo)bule components of our two-Sérsic galaxies. Bottom: distribution of the angular diameters of (pseudo)bule components. We do not show the distribution of disk Sérsic indices since they are fixed to $n = 1$.

illustrates that *HST* resolution is essential to disentangle and detect small (pseudo)bules in dwarf galaxies even

at low redshift ($z \lesssim 0.05$).

5.2. Irregular/Disturbed Dwarf Galaxies

Of the 41 dwarf galaxies in our sample, 6 (15%) have irregular/disturbed morphologies and were not successfully modeled in GALFIT (RGG 5, 40, 53, 66, 135 and 136). The *HST* galaxy images are shown in Figure 9. RGG 5, 40 and 136 do not have obvious photometric centers and resemble Magellanic-type dwarf irregulars. RGG 66 and 135 show signs of interactions/mergers, with RGG 135 displaying very elongated tidal tails. The remaining galaxy, RGG 53, looks more regular at first glance. However, a spiraled interior appears in the residuals when attempting to model the system in GALFIT. These galaxies are reminiscent of the dwarf galaxies found to host radio-selected AGNs by Reines et al. (2020), some of which host “wandering” (i.e., non-nuclear) BHs.

With the exception of RGG 5, the irregular/disturbed dwarf galaxies all fall in the composite region of the [OIII]/ $H\beta$ vs. [NII]/ $H\alpha$ narrow-line diagnostic diagram. RGG 5 falls in the AGN part of the diagram just above the maximum starburst line; however, it is difficult to reliably distinguish between AGN and star-formation in this low-metallicity region of the diagram (Groves et al. 2006). All of the galaxies were also selected to fall in the Seyfert region of the [OIII]/ $H\beta$ vs. [SII]/ $H\alpha$ diagram (see §2). Follow-up X-ray observations would help confirm if these irregular/disturbed dwarf galaxies do indeed host AGNs.

Figure 10 shows the distribution of physical resolutions probed at the distances of our galaxies. The irregulars tend to be relatively nearby. It is possible that AGNs in dwarf irregular galaxies are particularly difficult to identify at greater distances through optical selection since

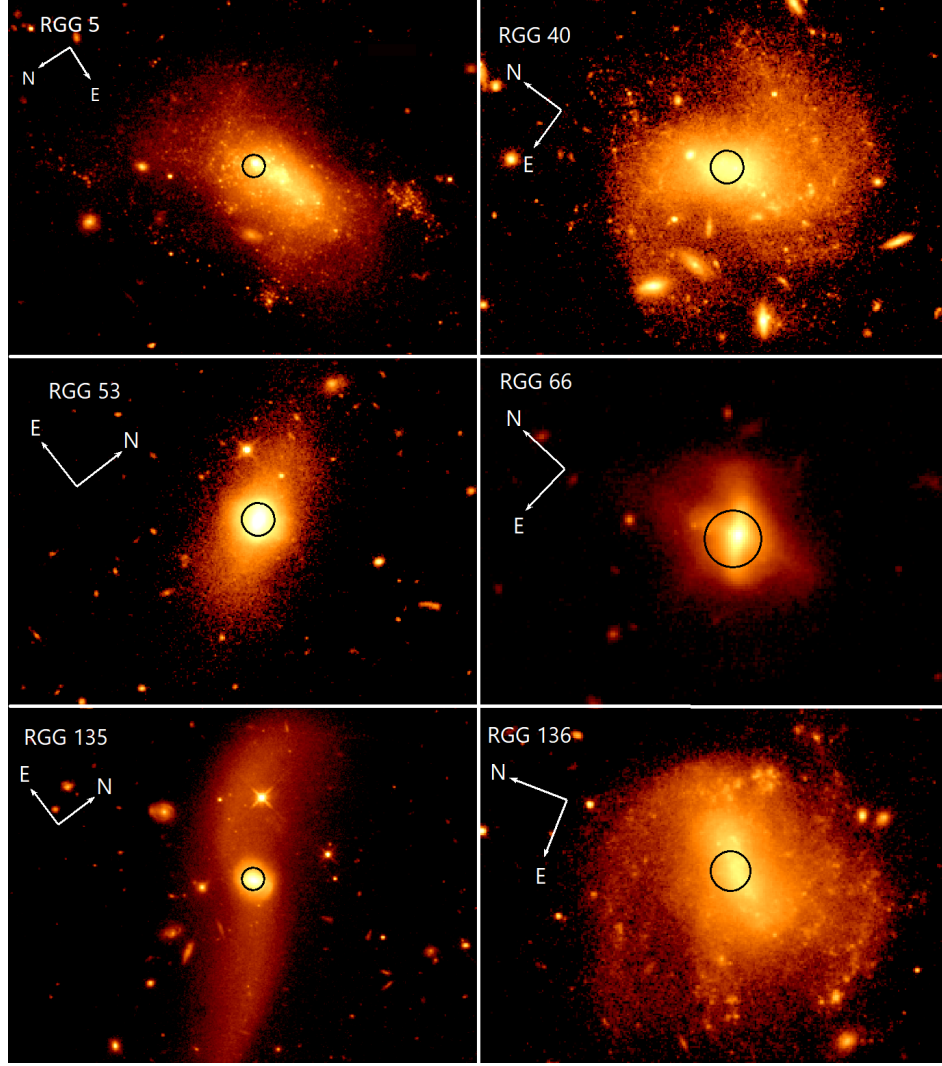


Figure 9. *HST* observations of the dwarf irregular galaxies in our sample shown on a log scale. Black circles indicate the locations of the SDSS spectroscopic fibers, which are $3''$ in diameter. Fiber positions were retrieved from the NASA Sloan Atlas (NSA). While no astrometric corrections have been applied to the *HST* images, we checked that our astrometry is consistent with the Hubble Legacy Archive.

more star-formation related emission can be included in the spectroscopic aperture. Indeed, Dickey et al. (2019) obtained Keck data of dwarf galaxies in the SDSS and found some to be classified as AGN with higher resolution data.

6. DISCUSSION

6.1. Comparison to Jiang et al. (2011)

Using *HST* observations, Jiang et al. (2011) studied the structures of 147 galaxies hosting low-mass BHs from the sample of Greene & Ho (2007). The objects in the Greene & Ho (2007) sample were selected as broad-line AGNs in the SDSS with virial BH masses $M_{\text{BH}} \lesssim 2 \times 10^6 M_{\odot}$. The hosts are sub- L_{\star} galaxies, yet they are more luminous and massive than the dwarfs studied here.

In some ways, our results are similar to those of Jiang et al. (2011). For example, most of their sample is dominated by disk galaxies with small bulge components. Our median B/T ratio of 0.21 ± 0.03 is comparable to the median B/T ratio of 0.18 reported by Jiang et al. (2011). They also found that the vast majority of these

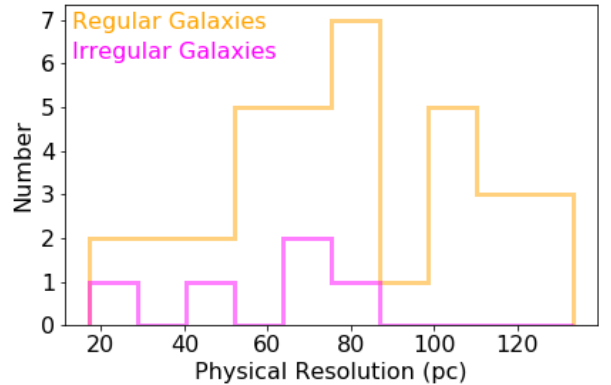


Figure 10. Distribution of the physical resolution at the various distances of the galaxies in this work, with *HST* angular resolution (FWHM) of $0''.13$. Regular galaxies are shown in orange histograms, while irregular galaxies are shown in magenta histograms.

bulges were likely to be pseudobulges, rather than classical bulges, which is in agreement with our results. Jiang

et al. (2011) report 70% of their modeled (pseudo)bulge components have a Sérsic index $n < 2$, and we find $\sim 81\%$ of our modeled (pseudo)bulges have a Sérsic index $n < 2$.

There are also notable differences between our sample of dwarf galaxies and the sample studied by Jiang et al. (2011). First, we see a very small fraction ($\sim 11\%$) of galaxies with bars. In contrast, Jiang et al. (2011) report a bar in $\sim 39\%$ of their sample. It has been postulated (e.g., Shlosman et al. 1989) that bars play a role in funneling gas to the centers of galaxies and feeding AGN. Our sample suggests there must be more at play than just bars. This same conclusion was reached by Jiang et al. (2011); despite their sample having a significant bar fraction, the fraction was still too low to suggest that bars alone feed AGN. Finally, in contrast with Jiang et al. (2011), we find dwarf irregular galaxies in our sample (§5.2).

6.2. Nature of the Point Sources: Nuclear Star Clusters and/or AGNs?

Here we consider the physical origin of the PSFs used in our models. Are the unresolved point sources dominated by the AGNs in the galaxies, or nuclear star clusters (NSCs)? The dwarf galaxies in our sample were selected to have optical signatures of AGNs (Reines et al. 2013), and $\sim 80\%$ of galaxies in this stellar mass range ($M_\star \sim 10^{8.5} - 10^{9.5} M_\odot$) are known to host NSCs (e.g., see Figure 3 in the review by Neumayer et al. 2020). Indeed, AGNs and NSCs are known to co-exist in many galaxies (Seth et al. 2008).

Both types of objects would appear as point sources in our *HST* WFC3 F110W images. The angular resolution is $0''.13$, corresponding to a physical resolution of ~ 70 pc at the median distance of our sample. Even in the nearest modeled galaxy in our sample (RGG 94, with a redshift of 0.0066), a point source corresponds to a physical size of $\lesssim 17$ pc. NSCs tend to have radii $\lesssim 10$ -15 pc (Geha et al. 2002; Neumayer et al. 2020), and therefore an NSC would likely appear as an unresolved source of light for all galaxies in our sample. Of course, continuum emission from AGNs would also be unresolved on these scales.

The F110W luminosities of the PSFs in our SNAP sample range from $10^{39.6}$ to $10^{42.1}$ erg s $^{-1}$, with a median of $\langle L_{\text{PSF}} \rangle = 10^{41.1}$ erg s $^{-1}$. We estimate the expected NSC luminosity in each galaxy using the scaling between galaxy stellar mass and NSC mass given by Neumayer et al. (2020):

$$\log M_{\text{NSC}} = 0.48 \times \log \left(\frac{M_\star}{10^9 M_\odot} \right) + 6.51 \quad (3)$$

Galaxy stellar masses are adopted from the NSA and given in Table 1. We estimate the F110W luminosity given the predicted NSC mass with Starburst99 models for the continuum (Leitherer et al. 1999), assuming an instantaneous burst and a metallicity of 0.008 as appropriate for these dwarfs (Reines et al. 2013).

We show the measured PSF luminosities in our galaxies versus the predicted luminosities for stellar populations (i.e., NSCs) of three different ages in Figure 11. The two older ages, 900 Myr and 100 Myr, are typical of NSCs (Neumayer et al. 2020), while 10 Myr would be an abnormally young age for an NSC. However, we include

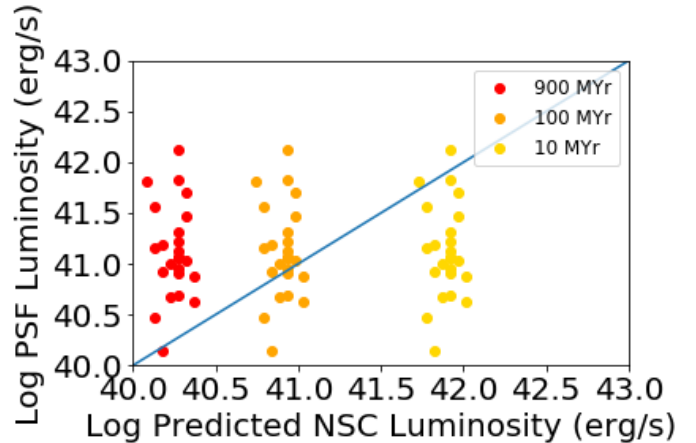


Figure 11. Central PSF luminosity for dwarf galaxies in our SNAP sample versus predicted NSC luminosity for various stellar population ages (see §6.2). The blue line shows the one-to-one relation.

the 10 Myr model because the most luminous observed PSFs are $\sim 10 - 100\times$ the predicted NSC luminosity unless we assume such a young cluster. This may suggest these simple stellar population models do not adequately represent NSCs, or that there is another contribution to the unresolved source of light (such as the AGN), at least for the most luminous PSFs. It is also possible that the scaling relation between NSC mass and stellar mass may be bimodal (as discussed in Ordenes-Briceño et al. 2018), rather than the relation in Equation 3.

Naively, we would not expect to detect continuum emission from the narrow-line AGNs in our SNAP sample, since the lack of detectable broad-line emission suggests that the nuclei are obscured. However, a nucleus could be unobscured, with the broad-line emission falling below the detection limit in the Reines et al. (2013) study. This scenario is exemplified by RGG 118, in which broad H α emission was not firmly detected in the SDSS spectrum, but was detected in follow up data with higher sensitivity and spectral resolution (Baldassare et al. 2015). It is also possible that the obscuring material is clumpy, keeping some sight lines to the nucleus open that could contribute to the continuum we are observing. Additionally, continuum emission via scattered light has been observed from obscured nuclei (Zakamska et al. 2005), which could be contributing to our point sources. There could also be some contribution at $1.1 \mu\text{m}$ from very hot dust.

6.3. Selection Effects

We note that our sample of AGN-hosting dwarf galaxies is not complete. The dwarf galaxies studied here were selected to have optical spectroscopic indications of an AGN (Reines et al. 2013). There are other ways to identify active BHs in dwarf galaxies - e.g., radio (Reines et al. 2011, 2014, 2020), X-ray (Lemons et al. 2015; Birchall et al. 2020), AGN variability (Baldassare et al. 2020), and the host properties can be quite different depending on the BH selection method (e.g., Reines et al. 2020).

As discussed in Reines et al. (2013), optical diagnostics are only sensitive to actively accreting BHs in galaxies with relatively low star formation. Even if accreting

at the Eddington limit, lower-mass BHs are not very luminous, leading to a selection bias towards dwarf galaxies hosting highly accreting BHs and/or more massive BHs. Emission lines from an AGN can also be hidden by host galaxy light even without significant star formation (Moran et al. 2002). Moreover, low-metallicity AGNs overlap with low-metallicity starbursts in the upper-left region of the BPT diagram (e.g., Groves et al. 2006; Yang et al. 2017). This will lead to a bias against actively star-forming dwarf galaxies, despite possibly hosting a massive BH (Reines et al. 2011; Riffel 2020; Birchall et al. 2020; Baldassare et al. 2020). The $3''$ -diameter SDSS fibers are three times the median angular effective diameter of the (pseudo)bulge components of our galaxies (median $2r_{e,\text{bulge}} = 1''$); therefore only galaxies which are AGN dominant and have bright, well-defined centers will be selected via SDSS spectroscopy (Reines et al. 2013).

In addition, many dwarf galaxies are simply too faint to be targeted for spectroscopy in the SDSS and even if they are, there is no guarantee the fiber placement coincides with a potential AGN. Instead, the spectroscopic fiber may be centered on a bright star forming region, and/or the BH may not reside in the nucleus (Reines et al. 2020). Therefore, while the Reines et al. (2013) sample is likely highly incomplete, the galaxies studied here are representative of that optically-selected sample of AGNs in dwarf galaxies (Figure 2).

6.4. Environmental Effects on Galaxy Morphologies

It has been observed that the environment around a galaxy plays a role in the morphology of the galaxy. Galaxies which are in less dense environments tend to be diskier, while galaxies in a more tightly packed environment tend to be rounder and more bulge-like (see, e.g. Rong et al. 2020).

For 28 of the dwarf galaxies in this work, the distance to the nearest massive host galaxy has been measured using the 2MASS Extended Source Catalog and taking redshifts from SDSS spectroscopy and several other sources (Geha et al. 2012). The remaining galaxies fall within one degree of the edge of the SDSS footprint, and so the environment was not analyzed. The nearest massive host galaxy was chosen to be the nearest galaxy with $M_{K_s} < -23$, and dwarfs were considered to be “isolated” by Geha et al. (2012) if the nearest massive host is more than 1.5 Mpc away. This is a conservative estimate of whether a galaxy is isolated or not; many galaxies less than 1.5 Mpc away from a more massive galaxy are still isolated, as they are often separated by many virial radii.

We show the B/T ratio plotted against the distance to the nearest host (DHOST) for the galaxies with environment data in Figure 12. We find that the majority of dwarfs in our sample do not meet the criterion to be considered isolated, but we do not find a correlation between whether the bulge or disk dominates and the isolation of the galaxy. For our sample, it may be difficult to disentangle the effects of hosting an AGN from the effects of the environment.

7. CONCLUSIONS

We have presented a study of 41 dwarf galaxies hosting optically-selected massive BHs (Reines et al. 2013) using *HST* near-infrared observations. In this first paper,

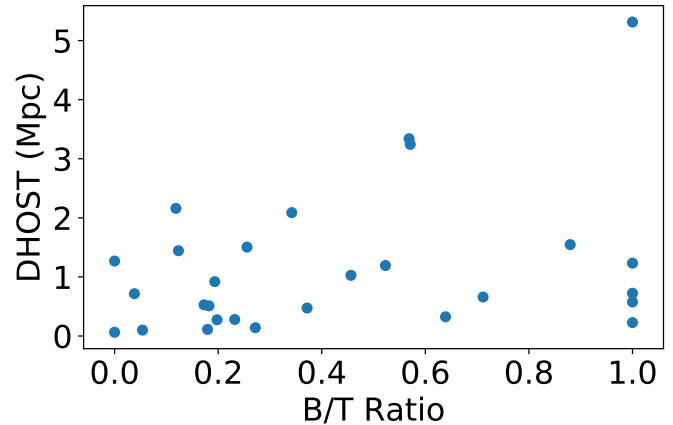


Figure 12. Distance from the dwarf galaxy to the nearest massive host versus the measured bulge to total light ratio.

we examine the morphologies and structural components of the host galaxies using the galaxy image fitting software GALFIT (Peng et al. 2010). We will compare these AGN-hosting dwarf galaxies to the general population of dwarf galaxies in a forthcoming paper. The main results of this work are summarized below:

1. The majority of the dwarf galaxies in our sample (85%) have regular morphologies, although there is a non-negligible fraction (15%) of irregular/disturbed galaxies in our sample (see Figure 9).
2. We perform 2D bulge-disk decompositions for the regular galaxies and find that the majority are disk-dominated with small pseudobulges. The median bulge-to-total light ratio is $\langle B/T \rangle = 0.21$.
3. Our sample also includes three dwarf disk galaxies without detectable bulges and six pure bulge/elliptical galaxies.
4. The best-fit models for the regular dwarf galaxies include a central point source of light. The point sources are consistent with originating from nuclear star clusters and/or AGNs.
5. Of the irregular/disturbed galaxies, three appear to be Magellanic-type dwarf irregulars and two exhibit obvious tidal features indicative of interactions/mergers.

We have shown that optically-selected BH-hosting dwarf galaxies exhibit a variety of morphologies and structures. This has important implications for constraining the BH occupation fraction at low mass, which is a key diagnostic for discriminating between BH seeding mechanisms (e.g., Volonteri 2010; Greene et al. 2019). While there have been valiant efforts to constrain the BH occupation fraction in low mass galaxies (Miller et al. 2015), studies that only focus on a particular type of dwarf galaxy (e.g., early-types) may well miss the bulk of the population.

We thank the anonymous referee for their helpful comments and questions during the review pro-

cess. SJK acknowledges support for this project provided by a fellowship from the Montana Space Grant Consortium. Support for Program number HST-GO-14251.004A was provided by NASA through a grant from the Space Telescope Science Institute, which is operated by the Association of Universities for Research in Astronomy, Incorporated, under NASA contract NAS5-26555. AER gratefully acknowledges support for this paper provided by NASA through EPSCoR grant number 80NSSC20M0231.

APPENDIX
HST IMAGES AND GALFIT MODELS

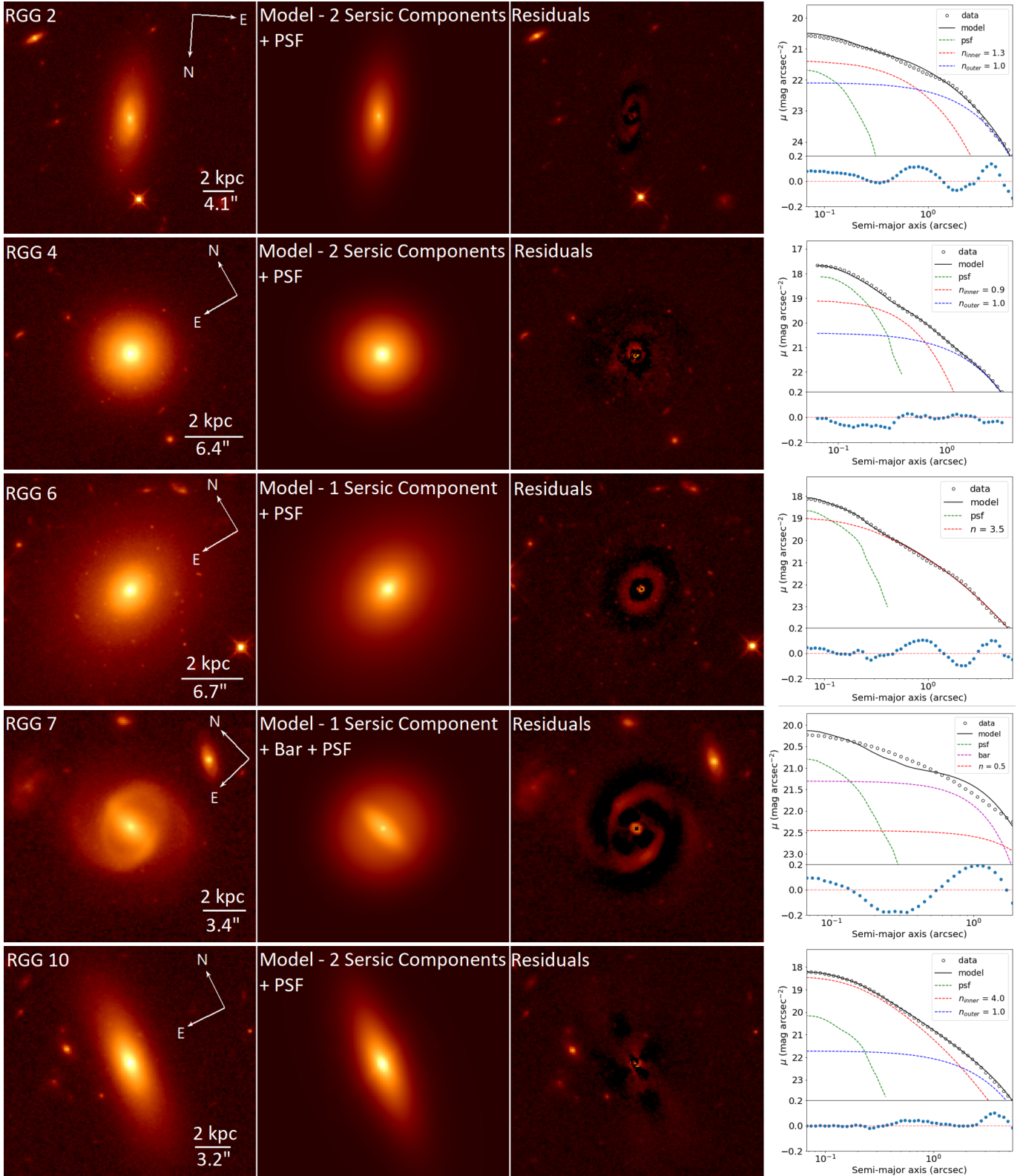


Figure 13. Left three panels: *HST* image, GALFIT model, and the residuals after subtracting the model from the image. Images are shown on a stretched log scale to show faint details in the residuals. Right: Surface brightness profiles. The data are shown as black circles and the model is shown as a black line. The individual model components are shown as colored dashed lines. The residuals are shown in the bottom panel.

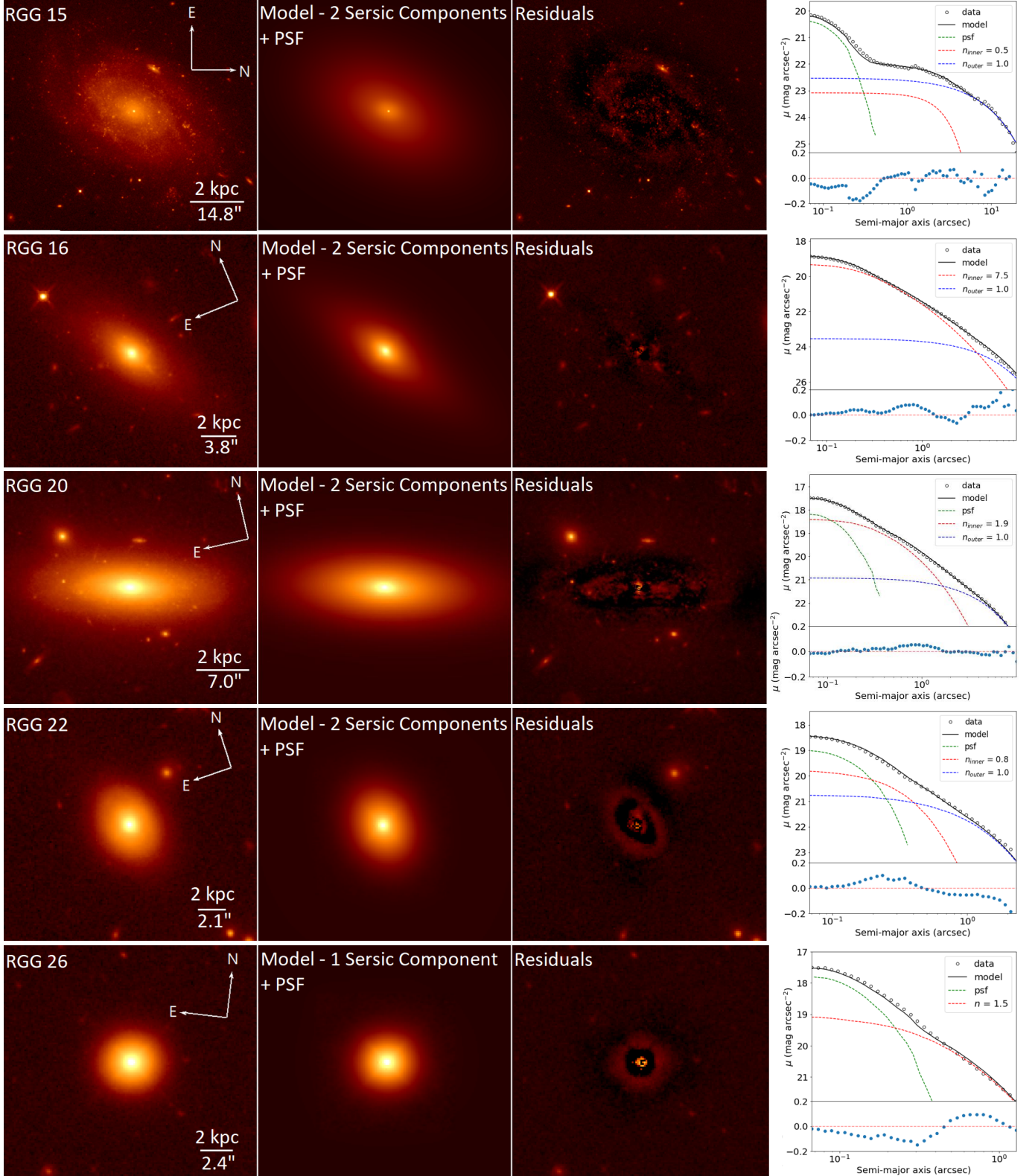


Figure 14. Left three panels: *HST* image, GALFIT model, and the residuals after subtracting the model from the image. Images are shown on a stretched log scale to show faint details in the residuals. Right: Surface brightness profiles. The data are shown as black circles and the model is shown as a black line. The individual model components are shown as colored dashed lines. The residuals are shown in the bottom panel.

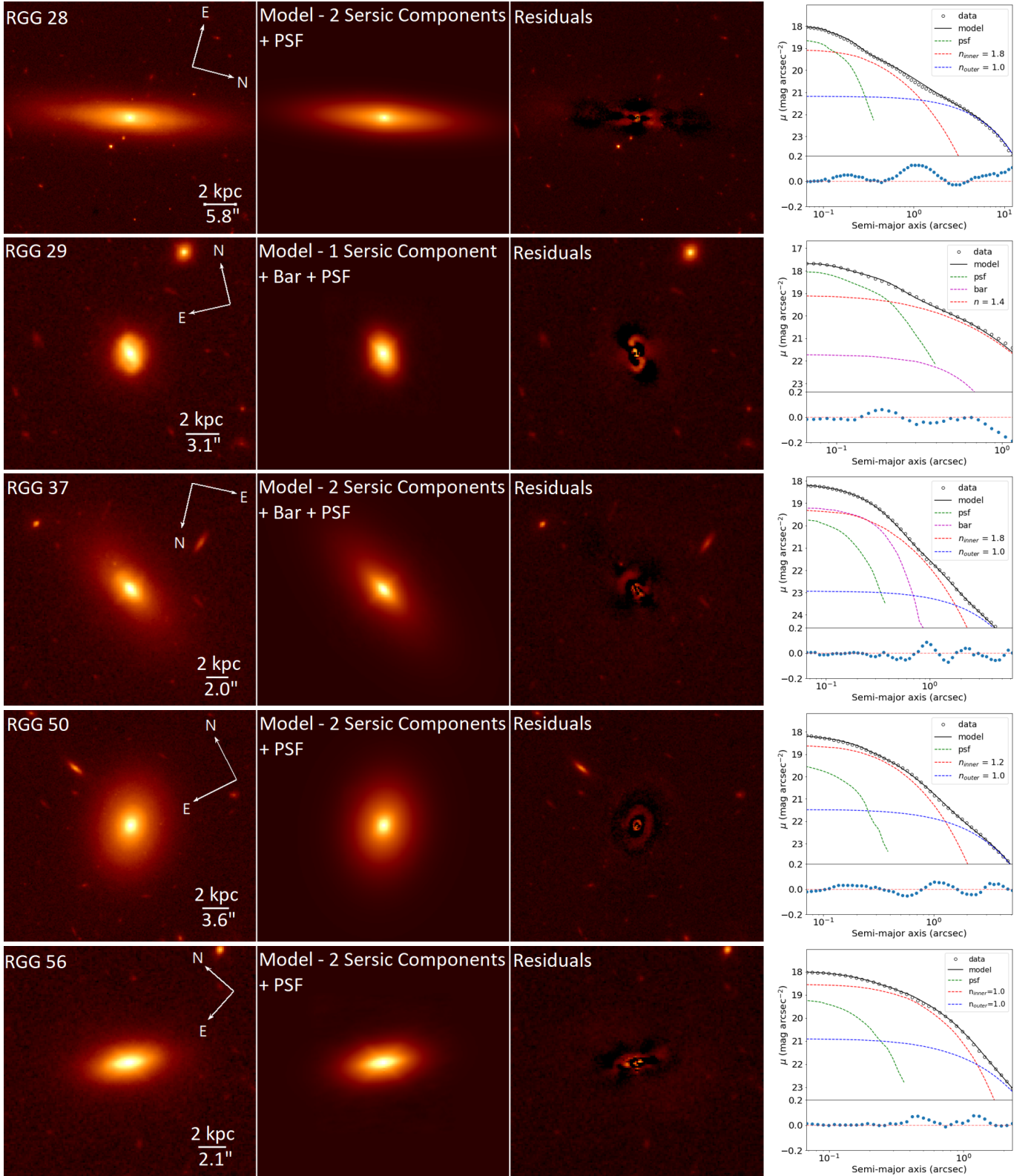


Figure 15. Left three panels: *HST* image, GALFIT model, and the residuals after subtracting the model from the image. Images are shown on a stretched log scale to show faint details in the residuals. Right: Surface brightness profiles. The data are shown as black circles and the model is shown as a black line. The individual model components are shown as colored dashed lines. The residuals are shown in the bottom panel.

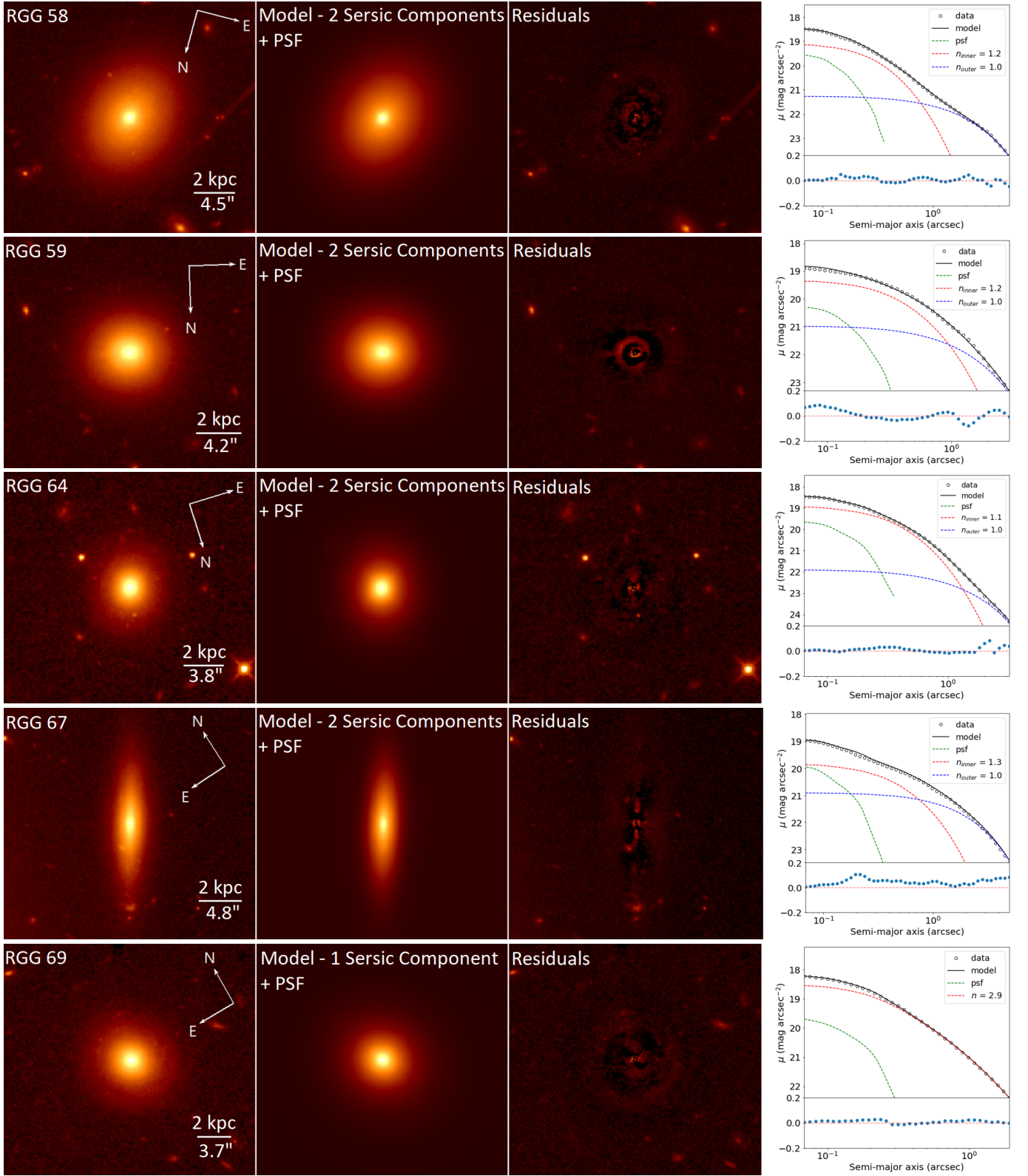


Figure 16. Left three panels: *HST* image, GALFIT model, and the residuals after subtracting the model from the image. Images are shown on a stretched log scale to show faint details in the residuals. Right: Surface brightness profiles. The data are shown as black circles and the model is shown as a black line. The individual model components are shown as colored dashed lines. The residuals are shown in the bottom panel.

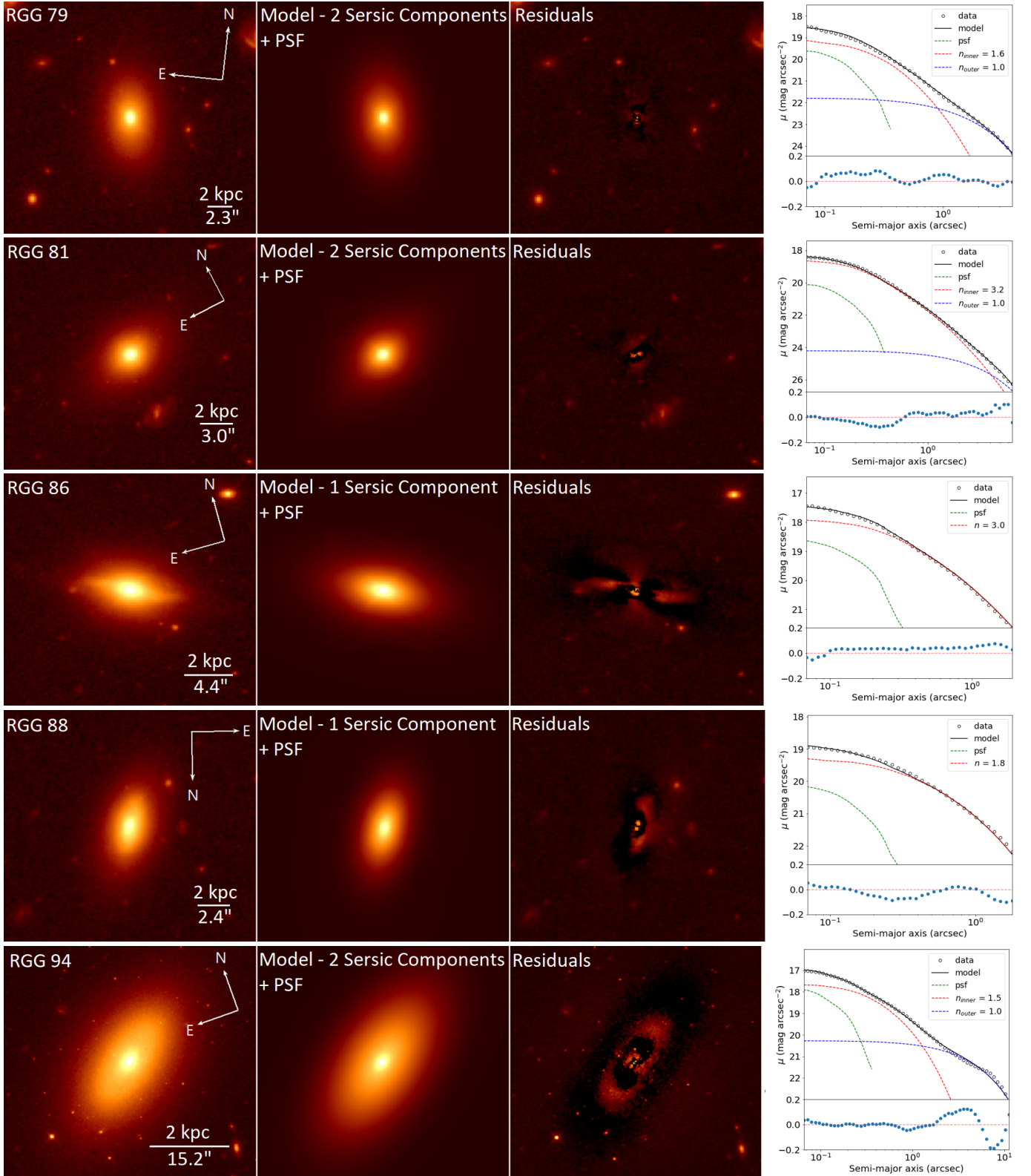


Figure 17. Left three panels: *HST* image, GALFIT model, and the residuals after subtracting the model from the image. Images are shown on a stretched log scale to show faint details in the residuals. Right: Surface brightness profiles. The data are shown as black circles and the model is shown as a black line. The individual model components are shown as colored dashed lines. The residuals are shown in the bottom panel.

Table 2
Fitting Results for Galaxies With Regular Morphologies

| RGG ID (1) | Component (2) | m_{F110W} (3) | n (4) | R_e (kpc) (5) | q (6) | Additional Components (7) |
|---------------------|------------------|--------------------|-----------------|--------------------|----------|------------------------------|
| RGG 1 ^a | PSF | 21.86 ± 0.02 | - | - | - | |
| | Inner Sérsic | 19.52 ± 0.23 | 0.32 ± 0.09 | 0.71 ± 0.03 | 0.51 | |
| | Outer Sérsic | 17.41 ± 0.06 | 0.83 ± 0.13 | 1.61 ± 0.03 | 0.72 | |
| RGG 2 | PSF | 23.9 ± 0.01 | - | - | - | |
| | Inner Sérsic | 20.3 ± 0.15 | 1.31 ± 0.01 | 0.73 ± 0.01 | 0.44 | - |
| | Outer Sérsic | 18.78 ± 0.10 | 1.00 | 2.16 ± 0.01 | 0.41 | - |
| RGG 4 | PSF | 20.41 ± 0.01 | - | - | - | |
| | Inner Sérsic | 19.22 ± 0.06 | 0.87 ± 0.01 | 0.13 ± 0.01 | 0.95 | |
| | Outer Sérsic | 17.67 ± 0.03 | 1.00 | 0.68 ± 0.01 | 0.99 | |
| RGG 6 | PSF | 20.99 ± 0.05 | - | - | - | |
| | Sérsic | 17.05 ± 0.10 | 3.52 ± 0.06 | 1.32 ± 0.04 | 0.81 | |
| RGG 7 | PSF | 23.07 ± 0.01 | - | - | - | |
| | Sérsic | 18.93 ± 0.02 | 0.52 ± 0.01 | 1.41 ± 0.01 | 0.96 | Bar ($m_{F110W} = 20.09$) |
| RGG 9 ^a | PSF | 21.86 ± 0.02 | - | - | - | |
| | Sérsic | 17.01 ± 0.04 | 2.30 ± 0.11 | 1.21 ± 0.26 | 0.86 | |
| RGG 10 | PSF | 22.39 ± 0.05 | - | - | - | |
| | Inner Sérsic | 18.51 ± 0.01 | 3.97 ± 0.78 | 0.72 ± 0.15 | 0.48 | |
| | Outer Sérsic | 19.13 ± 0.05 | 1.00 | 2.21 ± 0.09 | 0.29 | |
| RGG 11 ^a | PSF | 19.61 ± 0.03 | - | - | - | |
| | Inner Sérsic | 18.40 ± 0.23 | 2.40 ± 0.18 | 0.13 ± 0.02 | 0.96 | |
| | Outer Sérsic | 16.22 ± 0.18 | 1.69 ± 0.09 | 2.57 ± 0.30 | 0.78 | |
| RGG 15 | PSF | 22.54 ± 0.02 | - | - | - | |
| | Inner Sérsic | 19.8 ± 0.17 | 0.48 ± 0.01 | 0.33 ± 0.01 | 0.70 | |
| | Outer Sérsic | 16.3 ± 0.01 | 1.00 | 1.96 ± 0.01 | 0.64 | |
| RGG 16 | PSF | 22.17 ± 0.01 | - | - | - | |
| | Inner Sérsic | 18.52 ± 0.15 | 3.32 ± 0.22 | 0.98 ± 0.08 | 0.68 | |
| | Outer Sérsic | 19.50 ± 0.07 | 1.00 | 3.88 ± 0.04 | 0.30 | |
| RGG 20 | PSF | 20.45 ± 0.01 | - | - | - | |
| | Inner Sérsic | 17.94 ± 0.15 | 1.86 ± 0.01 | 0.33 ± 0.02 | 0.46 | |
| | Outer Sérsic | 16.87 ± 0.07 | 1.00 | 1.93 ± 0.02 | 0.36 | |
| RGG 22 | PSF | 21.18 ± 0.01 | - | - | - | |
| | Inner Sérsic | 20.55 ± 0.09 | 0.83 ± 0.05 | 0.28 ± 0.01 | 0.83 | |
| | Outer Sérsic | 18.9 ± 0.04 | 1.00 | 1.45 ± 0.03 | 0.78 | |
| RGG 26 | PSF | 20.08 ± 0.01 | - | - | - | |
| | Sérsic | 18.54 ± 0.01 | 1.54 ± 0.09 | 0.68 ± 0.01 | 0.91 | |
| RGG 28 | PSF | 20.86 ± 0.02 | - | - | - | |
| | Inner Sérsic | 18.54 ± 0.03 | 1.77 ± 0.02 | 0.38 ± 0.01 | 0.56 | - |
| | Outer Sérsic | 17.24 ± 0.02 | 1.00 | 2.83 ± 0.02 | 0.21 | |
| RGG 29 | PSF | 20.32 ± 0.01 | - | - | - | |
| | Sérsic | 18.97 ± 0.01 | 1.40 ± 0.06 | 0.47 ± 0.01 | 0.61 | Bar ($m_{F110W} = 22.26$) |
| RGG 32 ^a | PSF | 18.45 ± 0.03 | - | - | - | |
| | Inner Sérsic | 17.77 ± 0.25 | 1.62 ± 0.20 | 0.29 ± 0.02 | 0.90 | |
| | Outer Sérsic | 16.07 ± 0.10 | 0.74 ± 0.03 | 2.03 ± 0.01 | 0.95 | |
| RGG 37 | PSF | 21.96 ± 0.08 | - | - | - | |
| | Inner Sérsic | 19.50 ± 0.01 | 1.79 ± 0.16 | 0.66 ± 0.01 | 0.53 | Bar ($m_{F110W} = 20.66$) |
| | Outer Sérsic | 19.60 ± 0.28 | 1.00 | 4.27 ± 0.15 | 0.47 | |
| RGG 48 ^a | PSF | 21.55 ± 0.01 | - | - | - | |
| | Inner Sérsic | 19.75 ± 0.07 | 0.61 ± 0.08 | 0.29 ± 0.06 | 0.42 | |
| | Outer Sérsic | 16.64 ± 0.06 | 0.29 ± 0.01 | 2.12 ± 0.30 | 0.48 | |
| RGG 50 | PSF | 21.70 ± 0.10 | - | - | - | |
| | Inner Sérsic | 18.66 ± 0.21 | 1.24 ± 0.03 | 0.30 ± 0.01 | 0.77 | |
| | Outer Sérsic | 18.09 ± 0.17 | 1.00 | 1.86 ± 0.01 | 0.75 | |
| RGG 56 | PSF | 21.42 ± 0.01 | - | - | - | |
| | Inner Sérsic | 19.19 ± 0.01 | 1.04 ± 0.06 | 0.48 ± 0.01 | 0.26 | |
| | Outer Sérsic | 19.49 ± 0.02 | 1.00 | 1.48 ± 0.08 | 0.44 | |

Table 2 — *Continued*

| RGG ID (1) | Component (2) | m_{F110W} (3) | n (4) | R_e (kpc) (5) | q (6) | Additional Components (7) |
|----------------------|------------------|--------------------|-----------------|--------------------|------------|------------------------------|
| RGG 58 | PSF | 21.77 ± 0.01 | - | - | - | |
| | Inner Sérsic | 19.45 ± 0.07 | 1.19 ± 0.01 | 0.19 ± 0.01 | 0.85 | |
| | Outer Sérsic | 17.82 ± 0.04 | 1.00 | 1.49 ± 0.01 | 0.81 | |
| RGG 59 | PSF | 22.53 ± 0.01 | - | - | - | |
| | Inner Sérsic | 19.15 ± 0.15 | 1.19 ± 0.02 | 0.30 ± 0.01 | 0.83 | |
| | Outer Sérsic | 18.44 ± 0.07 | 1.00 | 0.96 ± 0.02 | 0.92 | |
| RGG 64 | PSF | 21.87 ± 0.02 | - | - | - | |
| | Inner Sérsic | 19.05 ± 0.14 | 1.13 ± 0.01 | 0.26 ± 0.01 | 0.87 | |
| | Outer Sérsic | 19.36 ± 0.20 | 1.00 | 1.13 ± 0.04 | 0.82 | |
| RGG 67 | PSF | 22.24 ± 0.01 | - | - | - | |
| | Inner Sérsic | 19.74 ± 0.15 | 1.29 ± 0.06 | 0.36 ± 0.01 | 0.66 | |
| | Outer Sérsic | 18.58 ± 0.07 | 1.00 | 1.38 ± 0.01 | 0.26 | |
| RGG 69 | PSF | 21.85 ± 0.01 | - | - | - | |
| | Sérsic | 17.89 ± 0.15 | 2.88 ± 0.13 | 0.69 ± 0.01 | 0.90 | |
| RGG 79 | PSF | 21.84 ± 0.02 | - | - | - | |
| | Inner Sérsic | 19.78 ± 0.18 | 1.61 ± 0.01 | 0.35 ± 0.01 | 0.66 | |
| | Outer Sérsic | 19.23 ± 0.09 | 1.00 | 2.17 ± 0.04 | 0.60 | |
| RGG 81 | PSF | 22.44 ± 0.13 | - | - | - | |
| | Inner Sérsic | 18.74 ± 0.13 | 3.17 ± 0.14 | 0.49 ± 0.01 | 0.87 | |
| | Outer Sérsic | 20.90 ± 0.01 | 1.00 | 2.99 ± 0.05 | 0.40 | |
| RGG 86 | PSF | 20.79 ± 0.22 | - | - | - | |
| | Sérsic | 17.68 ± 0.10 | 2.97 ± 0.15 | 0.56 ± 0.01 | 0.49 | |
| RGG 88 | PSF | 22.36 ± 0.22 | - | - | - | |
| | Sérsic | 18.70 ± 0.10 | 1.79 ± 0.05 | 0.98 ± 0.01 | 0.87 | |
| RGG 89 | PSF | 21.72 ± 0.01 | - | - | - | |
| | Inner Sérsic | 19.49 ± 0.02 | 1.39 ± 0.03 | 0.31 ± 0.01 | 0.88 | |
| | Outer Sérsic | 19.30 ± 0.02 | 1.00 | 1.42 ± 0.04 | 0.86 | |
| RGG 94 | PSF | 20.23 ± 0.01 | - | - | - | |
| | Inner Sérsic | 17.47 ± 0.02 | 1.45 ± 0.02 | 0.09 ± 0.01 | 0.68 | |
| | Outer Sérsic | 15.71 ± 0.02 | 1.00 | 0.94 ± 0.01 | 0.54 | |
| RGG 118 ^b | PSF | 24.26 ± 0.03 | - | - | - | |
| | Inner Sérsic | 20.55 ± 0.09 | 0.80 ± 0.10 | 1.57 ± 0.22 | 0.45 | |
| | Outer Sérsic | 18.66 ± 0.14 | 1.00 | 6.51 ± 1.72 | 0.69 | |
| RGG 119 ^a | PSF | 18.94 ± 0.07 | - | - | - | |
| | Inner Sérsic | 19.36 ± 0.21 | 2.55 ± 0.47 | 0.17 ± 0.01 | 0.46 | |
| | Outer Sérsic | 17.23 ± 0.05 | 0.91 ± 0.06 | 1.02 ± 0.01 | 0.78 | |
| RGG 123 ^c | PSF | 20.00 ± 0.2 | - | - | - | |
| | Sérsic | 17.53 ± 0.11 | 1.00 | 1.41 ± 0.09 | - | |
| RGG 127 ^a | PSF | 19.94 ± 0.01 | - | - | - | |
| | Inner Sérsic | 20.40 ± 0.01 | 0.95 ± 0.48 | 0.09 ± 0.02 | 0.53 | |
| | Outer Sérsic | 18.13 ± 0.05 | 0.70 ± 0.23 | 1.25 ± 0.02 | 0.68 | Bar ($m_{F110W} = 17.75$) |

Note. — Column 1: identification number given in Reines et al. (2013). Column 2: Components in best-fit GALFIT model. Column 3: Total apparent ST magnitude reported by GALFIT. Column 4: Sérsic index reported by GALFIT. Column 5: Effective radius reported by GALFIT, converted to kpc. Column 6: Axis ratio (b/a) reported by GALFIT. Column 7: Any additional component included in the best-fit model.

^a Fitting results from Schutte et al. (2019). Outer Sérsic indices were allowed to vary rather than being fixed at $n = 1$.

^b Fitting results from Baldassare et al. (2017). Magnitudes are in the WFC3/IR F160W filter.

^c Fitting results from Jiang et al. (2011). Magnitudes are in the WFPC2 F814W filter.

REFERENCES

- Akaike, H. 1974, *IEEE Transactions on Automatic Control*, 19, 716
- Anglés-Alcázar, D., Faucher-Giguère, C.-A., Quataert, E., et al. 2017, *MNRAS*, 472, L109
- Baldassare, V. F., Geha, M., & Greene, J. 2020, *ApJ*, 896, 10
- Baldassare, V. F., Reines, A. E., Gallo, E., & Greene, J. E. 2015, *ApJL*, 809, L14
- Baldassare, V. F., Reines, A. E., Gallo, E., & Greene, J. E. 2017, *The Astrophysical Journal*, 850, doi:10.3847/1538-4357/aa9067
- Baldassare, V. F., Reines, A. E., Gallo, E., & Greene, J. E. 2017, *ApJ*, 836, 20
- Baldwin, J. A., Phillips, M. M., & Terlevich, R. 1981, *PASP*, 93, 5
- Birchall, K. L., Watson, M. G., & Aird, J. 2020, *MNRAS*, 492, 2268
- Blanton, M. R., & Roweis, S. 2007, *AJ*, 133, 734
- de Vaucouleurs, G. 1948, *Annales d’Astrophysique*, 11, 247
- Dickey, C. M., Geha, M., Wetzel, A., & El-Badry, K. 2019, *ApJ*, 884, 180
- Fisher, D. B., & Drory, N. 2008, in *Astronomical Society of the Pacific Conference Series*, Vol. 396, *Formation and Evolution of Galaxy Disks*, ed. J. G. Funes & E. M. Corsini, 309
- Geha, M., Blanton, M. R., Yan, R., & Tinker, J. L. 2012, *ApJ*, 757, 85
- Geha, M., Guhathakurta, P., & van der Marel, R. P. 2002, *AJ*, 124, 3073
- Ghez, A. M., Salim, S., Weinberg, N. N., et al. 2008, *ApJ*, 689, 1044
- Graham, A. W., & Guzmán, R. 2003, *AJ*, 125, 2936
- Greene, J. E. 2012, *Nature Communications*, 3, 1304 EP , review Article
- Greene, J. E., & Ho, L. C. 2005, *ApJ*, 630, 122
- . 2007, *ApJ*, 670, 92
- Greene, J. E., Strader, J., & Ho, L. C. 2019, *arXiv e-prints*, arXiv:1911.09678
- Groves, B. A., Heckman, T. M., & Kauffmann, G. 2006, *MNRAS*, 371, 1559
- Habouzit, M., Volonteri, M., & Dubois, Y. 2017, *MNRAS*, 468, 3935
- Jiang, Y.-F., Greene, J. E., Ho, L. C., Xiao, T., & Barth, A. J. 2011, *ApJ*, 742, 68
- Kauffmann, G., Heckman, T. M., Tremonti, C., et al. 2003, *Monthly Notices of the Royal Astronomical Society*, 346, 1055
- Kewley, L. J., Dopita, M. A., Sutherland, R. S., Heisler, C. A., & Trevena, J. 2001, *ApJ*, 556, 121
- Kewley, L. J., Groves, B., Kauffmann, G., & Heckman, T. 2006, *Monthly Notices of the Royal Astronomical Society*, 372, 961
- Kormendy, J., & Ho, L. C. 2013, *ARA&A*, 51, 511
- Kormendy, J., & Kennicutt, Jr., R. C. 2004, *ARA&A*, 42, 603
- Kormendy, J., & Richstone, D. 1995, *ARA&A*, 33, 581
- Leitherer, C., Schaerer, D., Goldader, J. D., et al. 1999, *ApJS*, 123, 3
- Lemons, S. M., Reines, A. E., Plotkin, R. M., Gallo, E., & Greene, J. E. 2015, *ApJ*, 805, 12
- Miller, B. P., Gallo, E., Greene, J. E., et al. 2015, *ApJ*, 799, 98
- Moran, E. C., Filippenko, A. V., & Chornock, R. 2002, *ApJL*, 579, L71
- Mortlock, D. J., Warren, S. J., Venemans, B. P., et al. 2011, *Nature*, 474, 616
- Neumayer, N., Seth, A., & Böker, T. 2020, *A&A Rev.*, 28, 4
- Nguyen, D. D., Seth, A. C., Neumayer, N., et al. 2019, *The Astrophysical Journal*, 872, 104
- Oh, S., Greene, J. E., & Lackner, C. N. 2017, *ApJ*, 836, 115
- Ordenes-Briceño, Y., Puzia, T. H., Eigenthaler, P., et al. 2018, *ApJ*, 860, 4
- Peng, C. Y., Ho, L. C., Impey, C. D., & Rix, H.-W. 2010, *AJ*, 139, 2097
- Reines, A. E., & Comastri, A. 2016, *Publications of the Astronomical Society of Australia*, 33, e054
- Reines, A. E., Condon, J. J., Darling, J., & Greene, J. E. 2020, *ApJ*, 888, 36
- Reines, A. E., Greene, J. E., & Geha, M. 2013, *ApJ*, 775, 116
- Reines, A. E., Plotkin, R. M., Russell, T. D., et al. 2014, *ApJL*, 787, L30
- Reines, A. E., Sivakoff, G. R., Johnson, K. E., & Brogan, C. L. 2011, *Nature*, 470, 66
- Reines, A. E., & Volonteri, M. 2015, *ApJ*, 813, 82
- Riffel, R. A. 2020, *MNRAS*, 494, 2004
- Rong, Y., Dong, X.-Y., Puzia, T. H., et al. 2020, *ApJ*, 899, 78
- Schutte, Z., Reines, A. E., & Greene, J. E. 2019, *ApJ*, 887, 245
- Sérsic, J. L. 1963, *Boletín de la Asociacion Argentina de Astronomia La Plata Argentina*, 6, 41
- Seth, A., Agüeros, M., Lee, D., & Basu-Zych, A. 2008, *ApJ*, 678, 116
- Shlosman, I., Frank, J., & Begelman, M. C. 1989, *Nature*, 338, 45
- Vito, F., Brandt, W. N., Yang, G., et al. 2017, *Monthly Notices of the Royal Astronomical Society*, 473, 2378
- Volonteri, M. 2010, *The Astronomy and Astrophysics Review*, 18, 279
- Volonteri, M., & Reines, A. E. 2016, *ApJL*, 820, L6
- Yang, H., Malhotra, S., Rhoads, J. E., & Wang, J. 2017, *ApJ*, 847, 38
- Zakamska, N. L., Schmidt, G. D., Smith, P. S., et al. 2005, *AJ*, 129, 1212